PROCEEDINGS OF SCIENCE

Atmospheric Monitoring for Astroparticle Physics Observatories

Bianca Keilhauer[a,*]

[a] *Karlsruhe Institute of Technology (KIT), Institute for Astroparticle Physics (IAP)*
PO Box 3640, 76021 Karlsruhe, Germany

E-mail: bianca.keilhauer@kit.edu

For many observatories recording high-energy cosmic rays, gamma rays, or neutrinos, the Earth's atmosphere is either an integral part or at least a considerable aspect of the detector setup. After giving an overview of the influence of the atmosphere and its variability on the development of the observed particle cascades and the signals detected from them, atmospheric monitoring strategies implemented by the different observatories are described. Examples of the impact of atmospheric parameters and profiles on the core data of these observatories are given and technical aspects of long-term and partially very laborious monitoring efforts of the Earth's atmosphere are discussed. Due to the per se interdisciplinary character of atmospheric monitoring in astroparticle physics, several new projects beyond the core physics of the astroparticle physics observatories have evolved and some are reviewed in this presentation.

38th International Cosmic Ray Conference (ICRC2023)
26 July - 3 August, 2023
Nagoya, Japan

*Speaker

PoS(ICRC2023)021

1. Introduction

In high-energy astroparticle physics, the atmosphere is an integral part of our observatories for detecting cosmic rays, gamma rays, and neutrinos. Depending on the applied detection technique, different aspects of the varying conditions in the atmosphere alter either the signal to be detected, the detector response to the signal, or both. The overall vertical structure of the atmosphere has to be considered, as well as the local and temporal variation, both on very different scales, of atmospheric conditions. Some of these variations and their effects on our observations can be investigated once for the site and purpose of the observatory, while other variations have to be monitored throughout observation periods. Since most of the observatories in astroparticle physics are operated for many years up to a few decades, atmospheric monitoring imposes a serious challenge on the operation effort and the instruments applied [1].

2. Detector techniques and their atmospheric dependences

High-energy cosmic rays can be detected in terms of their longitudinal development in the atmosphere and as a snapshot of their lateral particle distribution at some gound level. Typical particle detectors at ground are scintillator or water-Cherenkov detectors forming an array of several hundred to thousand km^2. The detectors consist of stations of the order of m^2 in size and are distributed in a large number over a large area with spacing of about $1-2$ km, see for examples the Telescope Array experiment [2], the IceTop array of IceCube [3], or the Pierre Auger Observatory [4]. Currently running cosmic-ray observatories co-operate fluorescence telescopes with such ground arrays for detecting the longitudinal light emission of cosmic-ray induced extensive air showers (EAS) [4, 5]. Also radio anntennas can observe the lateral footprint of the electromagnetic emission of EAS at a given ground level, see for examples the LOFAR experiment [6] or the AERA array at the Auger Observatory [7]. High-energy gamma-rays can be detected with Cherenkov telescopes, e.g. H.E.S.S. [8], MAGIC [9], or CTA [10]. The gamma-ray induced extensive air showers generate a small cone of Cherenkov light in the forward direction of the shower along the longitudinal development by its charged particles. The light emissions of ultrahigh-energy cosmic rays and neutrinos can also be observed by air-borne instruments. First tests and future missions are described in e.g. [11, 12], but not discussed here for its atmospheric monitoring concepts.

2.1 Particle detectors at ground

The particle interactions in the longitudinal development of EAS are affected by the state variables pressure P, temperature T, and the density ρ of the atmosphere. Mostly, the electromagnetic and muonic components are modified which results in different signals at ground. Higher pressure at ground is equivalent to higher amount of matter traversed by the EAS particles, varying the stage of the EAS development when it reaches the ground. The air density at about two radiation lengths above ground influences the Molière radius of the electromagnetic shower component and therefore the width of the lateral extent of the EAS at ground [13]. In a simulation study for the conditions at the Auger Observatory, the different signals in the water-Cherenkov detectors due to different atmospheric profiles in the seasons have been investiged, Fig. 1. It can be seen that EAS have a

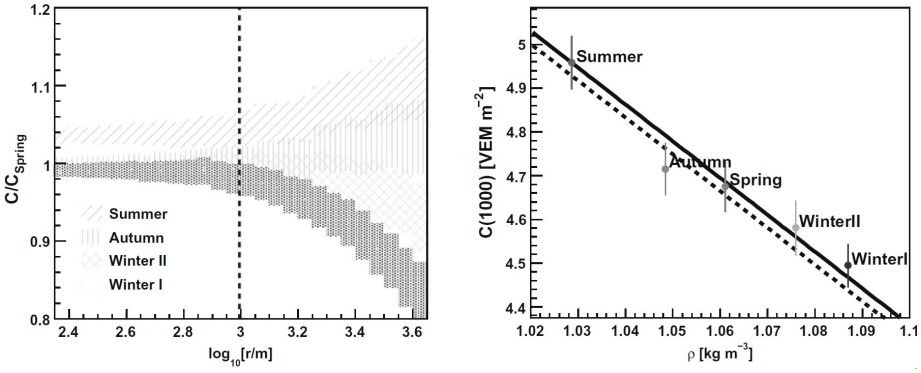

Figure 1: Left: Lateral distribution of the signal per unit area perpendicular to the shower axis of the water-Cherenkov detector at ground. Proton simulated EAS with $E = 10^{19}$ eV and $\theta = 18°$, for atmospheric conditions as parametrized for the Auger Observatory, normalised to the spring atmosphere. Right: Signal at 1000 m from the EAS core as a function of the air density ρ for the five exemplary atmospheric conditions. The dashed and continuous lines are the fit representations for two pressure conditions, $P = 856$ hPa and $P = 862$ hPa, respectively. From [13].

larger lateral extend during summer conditions and are narrower during winter. Significant modulations of the rate of events have been observed, both on a seasonal scale ($\approx 10\%$) and on a daily scale ($\approx 2\%$). Applying parametrized corrections to the detector signals including actual values for the respective atmospheric state conditions reduces the systematic uncertainties in the energy reconstruction of those EAS, and improves the accuracy for large scale anisotropy studies [13].

2.2 Fluorescence telescopes

Detecting the fluorescence emission incuded by EAS with telescopes is an almost model-independent technique for determining the energy of cosmic rays. Furthermore, it allows for a reliable estimate of the composition of cosmic rays by measuring the atmospheric depth of the EAS maximum $X_{\max}$. However, this technique is mostly affected by the atmosphere and its variability.

Longitudinal shower development The longitudinal shower development in the Earth's atmosphere can be described by the number of particles and by the energy deposit in air. Mainly the air density affects the particle interactions and decay probabilities. This can be reasonably described by an average vertical density profiles of the atmosphere if the longitudinal development is given as a function of atmospheric depth. Local and seasonal variations of the density profiles cause only minor modulations of the e.g. energy deposit, Fig. 2, left. For studying the expected signals of fluorescence telescopes, the fixed geometry of the field of view has to be considered. The vertical profile of atmospheric depth has to be converted into geometrical height, based on the air density profile. In Fig. 2, right, the deposited energy of a simulated Fe-induced EAS with 10^{19} eV and 60° inclination as a function of height is shown for three atmospheric conditions. The different positions of the shower maximum are marked and clearly observable with fluorescence telescopes [14]. Since the position of shower maximum is used as an indicator for the particle type of the cosmic ray, the extend of the atmospheric effect is illustrated in Fig. 3. If EAS would be observed in the reference US Standard Atmosphere, p-induced showers would in average penetrate deeper into the

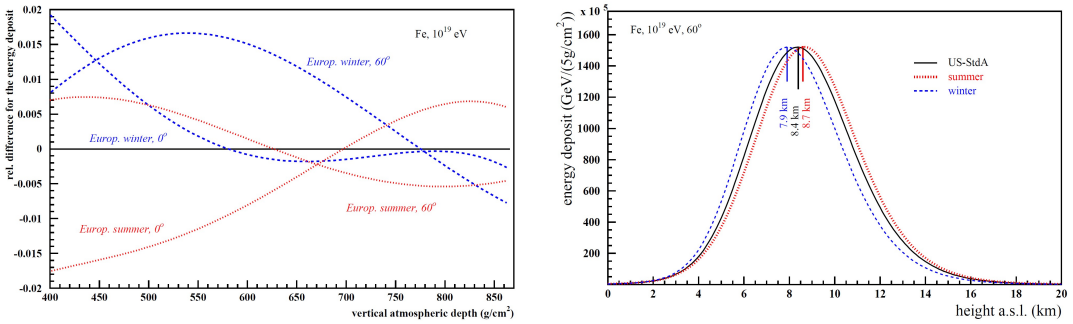

Figure 2: Left: Relative differences for the energy deposit simulated in European atmospheres for Fe-induced EAS with vertical and 60° inclination compared with the US Standard Atmosphere. Right: Longitudinal development of the energy deposit vs. height. From [14].

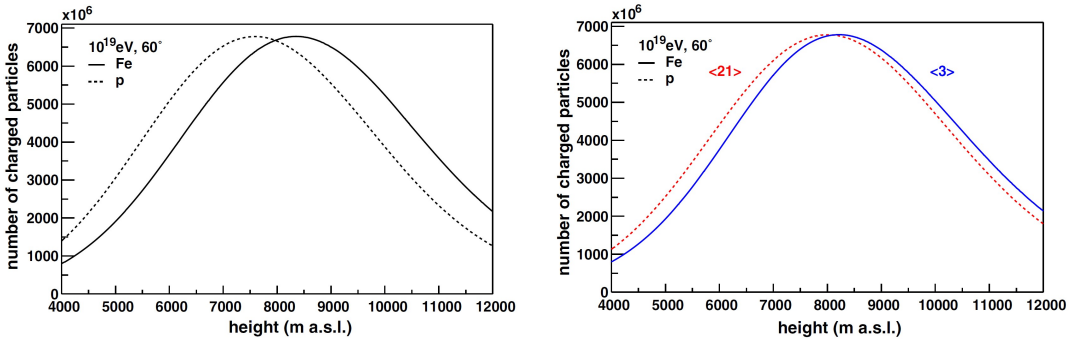

Figure 3: Profiles of charged particles. Left: For p- and Fe-induced EAS in the US Standard Atmosphere. Right: For p-induced EAS in Argentine summer, indicated by ⟨21⟩, and Fe-induced EAS in Argentine winter, indicated by ⟨3⟩. All EAS are simulated with 10^{19} eV and 60° inclination. From [15].

atmosphere than Fe-induced, Fig. 3, left. However comparing a p-induced EAS during summer conditions with an Fe-induced one during winter conditions, the previous clear separation of $X_{\max}$ would be obscured, Fig. 3, right.

Fluorescence light emission The energy deposit of EAS in the air causes an excitation of mainly nitrogen molecules. The subsequent disexcitation is partically happening by the emission of fluorescence light. This light is emitted isotropically and for the most prominent bands of N_2 and N_2^+ in the wavelengths range between about $\lambda = 280 - 420$ nm, cf. [16, 17]. The radiative de-excitation is competing with quenching processes by further molecules. The intial excitation of nitrogen is independent of the air conditions, but all the subsequent de-excitation processes are affected by the surrounding pressure P, temperature T, and particle content. A typical representation of the resulting fluorescence yield Y_{air} with its atmospheric dependences by introducing a reference pressure P', at which the probability of collisional quenching equals that of the radiative de-excitation, can be written as, cf. [18, 19],

$$Y_{\text{air}}(\lambda, P, T) = Y_{\text{air}}(337\text{nm}, P_0, T_0) \cdot \frac{I_\lambda}{I_{337}(P_0, T_0)} \cdot \frac{1 + \frac{P_0}{P'_{\text{air}}(\lambda, T_0)}}{1 + \frac{P}{P'_{\text{air}}(\lambda, T_0) \cdot \sqrt{\frac{T}{T_0}} \cdot \frac{H_\lambda(T_0)}{H_\lambda(T)}}}. \quad (1)$$

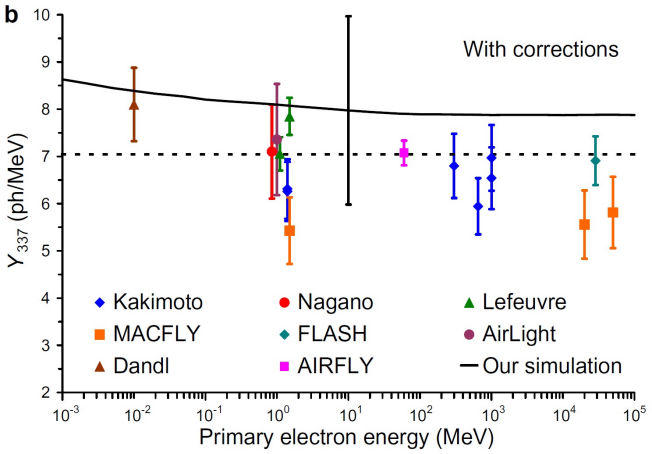

Figure 4: Fluorescence yield measurements normalized to common conditions (337 nm band in air at 800 hPa and 293 K). Some of the shown measurements were corrected for a bias in the energy deposition. The dashed line represents the average fluorescence yield of 7.04 photons/MeV as determined in [21] for the displayed experiments. The solid line represents the theoretical prediction of the absolute yield from simulations as described in the same work. From [21].

$Y_{\text{air}}(337\text{nm}, P_0, T_0)$ is the absolut yield of the reference emission of the most prominent de-excitation band of N_2 at 337 nm, given at the conditions P_0 and T_0. The strengths of the further emission bands are given in the second term. The pressure dependence in dry air is given by $1/P'_{\text{air}}(\lambda, T_0)$, and the temperature-dependent collisional cross sections between excited nitrogen and air molecules in general is given by

$$\frac{H_\lambda(T)}{H_\lambda(T_0)} = \left(\frac{T}{T_0}\right)^{\alpha_\lambda} \tag{2}$$

with α_λ being the exponent of the power law describing the temperature-dependent collisional cross sections for each wavelength. With finally replacing $1/P'_{\text{air}}$ in the denomiator of Eq. 1 with

$$\frac{1}{P'_{\text{air}}} \rightarrow \frac{1}{P'_{\text{air}}}\left(1 - \frac{e}{P}\right) + \frac{1}{P'_{\text{H}_2\text{O}}}\frac{e}{P}, \tag{3}$$

the additional quenching due to water vapor in humid air with a partial pressure of water vapor e is taken into account.

The fluorescence yield, in particular the absolute value for the most prominent emission at 337 nm, has been studied by many laboratory experiments over the last decades [20, 21]. A comparison of the recent experimental data along with a simulation study is shown in Fig. 4. A representation of the air fluorescence spectrum is given in Fig. 5, left. Comparing fluorescence spectra as measured by several experiments, different strengths of emission bands can be found and also small differences in the sum of the fluorescence yield in the wavelength range of interest, Fig. 5, right. For taking into account the atmospheric dependences of the non-radiative de-excitation processes, parameters for describing the pressure dependence, the humidity quenching, and the temperature-dependent collisional cross sections have to be found. Each of these effects has its own set of parameters and it is assumed that all individual transitions starting at the same upper vibrational level have the same parameter, cf. [19, 23]. Since laboratory experiments typically

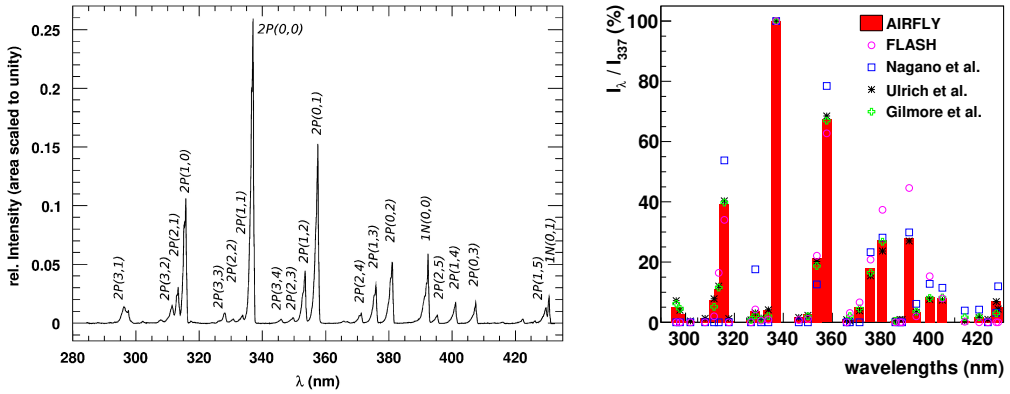

Figure 5: Left: Air fluorescence spectrum excited by 3 MeV electrons at 800 hPa. From [22]. Right: Relative fluorescence intensities between about 300 and 430 nm. The sum of the fluorescence yield in this wavelength range differs up to 3% compared to the yield obtained by AIRFLY. From [19].

measure the effects for each wavelength, where emissions at several wavelengths are coming from the same upper vibrational level, weighted averages for the parameters measured for bands of a particular molecular system with the same starting level are determined for the entire set of parameters in a common fluorescence description. The full set of parameters is listed in e.g. [23]. An illustration of the atmospheric dependences of the fluorescence emission is given in Fig. 6 for an exciting electron of 0.85 MeV in different atmospheric conditions. The reference atmosphere is the US Standard Atmosphere with exponential decreasing pressure, without any water vapor content, and a temperature profile which is linear decreasing up to 11 km a.s.l., constant at 216.65 K in the tropopause up to 20 km a.s.l., and followed by increasing temperatures in the stratosphere. It can be seen that in the troposphere the decreasing pressure with altitude yields an increasing light emission because of decreasing collisional quenching rates. Including the temperature-dependent collisional cross sections, the light emission becomes almost constant in the troposhpere and lower tropopause, because of the decreasing temperature resulting in decreasing collisional cross sections. Water vapor quenching is only relevant in the lowest kilometers of the atmoshpere, and only during warm conditions, when the absolute vapor content in air becomes relevant.

At the cosmic ray observatories operating fluorescence telescopes, usually different descriptions of the fluorescence light emission with different grades of detail are applied in the air shower reconstruction, which is one source of possible systematic differences in the primary energy and type determination between the results of these observatories.

Light transmission towards telescopes On its way from emission along the EAS development towards the telescope, the UV fluorescence light is attenuated by interactions with the molecular and aerosol components of the atmosphere. This attenuation is typically a combination of absorption and scattering processes. For the given wavelength range of the nitrogen fluorescence and the field of view of the telescopes for cosmic ray detection, absorption processes can be neglected, cf. [25]. The scattering processes can be treated separately, once for the scattering at molecules of air, so-called Rayleigh scattering, and for the scattering at aerosols in the air, so-called Mie scattering. Rayleigh scattering can be analytically described very well, given that the chemical

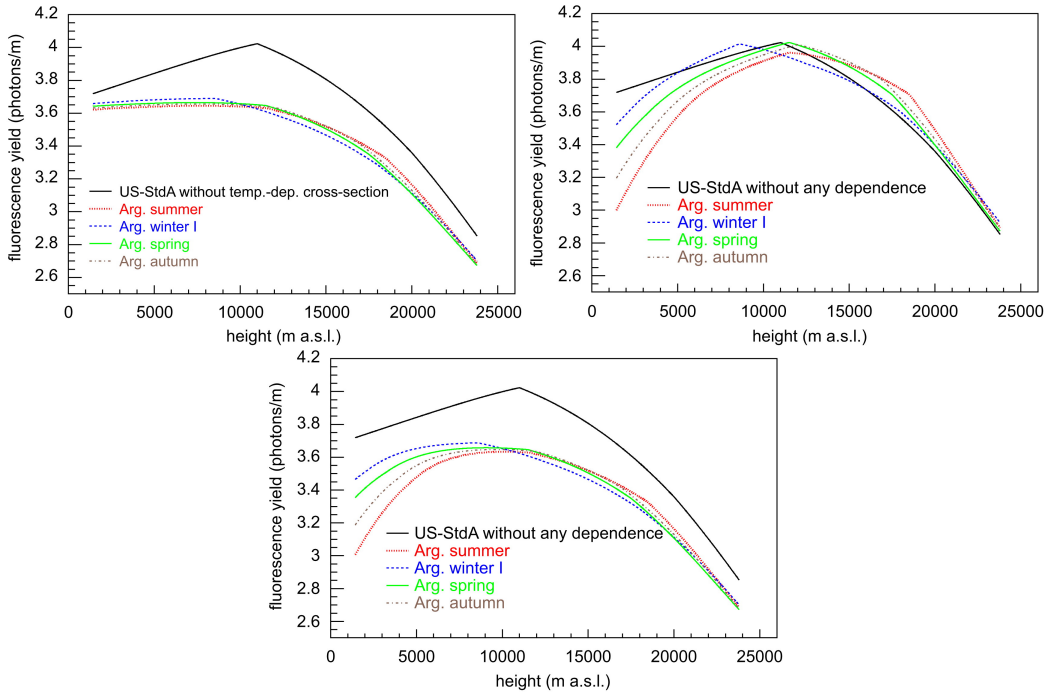

Figure 6: Fluorescence yield profiles for a 0.85 MeV electron. Upper left: In different atmospheric conditions in Argentina at the site of the Auger Observatory, including pressure dependence and temperature-dependent collisional cross sections. Upper right: With included pressure dependence and water vapor quenching. Bottom: Including all three atmospheric dependences. From [24].

compositon of the atmosphere can be considered as almost constant up to the mesopause and a proper analytic description of the vertical profile of the refractive index of air in dependence on pressure and temperature, cf. [25] and references therein. Scattering at aerosols is more complex and the transparency of the atmosphere at the sites of cosmic ray observatories is usually measured, cf. [26]. Apart from regular measurements for recording the actual amount and coarse-type in the atmosphere at the observatories, general characteristics of the aerosol scattering can be determined once for the conditions at an observatory with sufficient precision. For example, the Auger Observatory has determined the Ångström exponent of the parameterization for the wavelength dependence over few years with a Horizontal Attenuation Monitor, and the backscattering and asymmetry parameters of the phase function for describing the angular dependence of the aerosol scattering with an Aerosol Phase Function monitor [4, 25]. The averages of these measurements are implemented in the light transmission calculations since then. Overall, the attenuation due to Rayleigh scattering is much stronger than that caused by aerosol scattering, see Fig. 7. Even though its effect on the light transmission is larger, the Rayleigh scattering does not vary very much throughout a year, e.g. for conditions in Argentina at the Auger Observatory the annual variability is below about 1% [14]. The variability of the aerosol scattering is much higher and can be up to almost 90% [26]. Significant differences in the aerosol scattering appear within years, but also from year to year [28]. Even significant differences of the order of tens percent were measured within few nights. For the reconstruction of EAS, optical conditions of better than 0.1 for the vertical aerosol optical depth are required [27, 28].

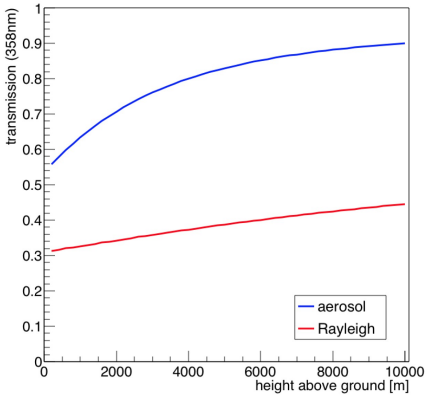

Figure 7: Optical transmission of a central wavelength in the nitrogen fluoresence spectrum for an EAS at 20 km distance. Rayleigh and Mie transmission factors are shown from the shower axis to a telescope. For the Mie scattering, a typical value of vertical aerosol optical depth VAOD(3km) = 0.04 is chosen. From [27].

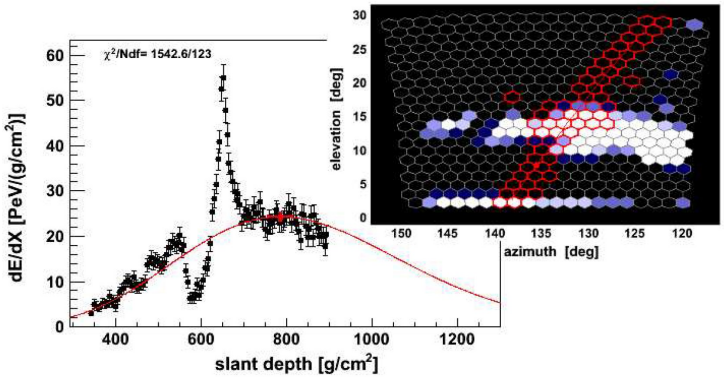

Figure 8: The upper right part gives an event display of a pixeled telescope for an EAS. Pixels which are triggered by light from the EAS are indicated in red. Information from an IR cloud camera is overlaid and pixels marked as cloudy are white or blueish. A reconstruction of the EAS in terms of its energy deposit vs. atmospheric depth is given in the lower left. Parts of the EAS profile show reduced signals, because of cloud, but some other parts show enhanced signals because of multiple scattering. From [29].

Clouds Clouds in the field of view of fluorescence telescopes alter the light transmission from the EAS towards the telescope. The light can be blocked entirely, reduced to some degree, or being enhanced because of different scattering. An example of an EAS profile detected by a fluorescence telescope affeced by cloud is shown in Fig. 8. Detecting clouds in cosmic ray observatories is particularly challenging. The used fluroscence detectors have a large field of view and clouds vary very much in size, shape, optical thickness, and altitude. For an optimal reconstruction of EAS, cloud information would be needed for every pixel of the fluorescence detector for all observation periods, but not only the information cloud – yes or no –, but in addition the position of the cloud in the respective field of view of the pixel.

2.3 Cherenkov telescopes

Imaging atmospheric Cherenkov telescopes are used for ground-based gamma-ray astrophysics. The telescopes detect gamma-ray induced air showers via their emission of Cherenkov light. The

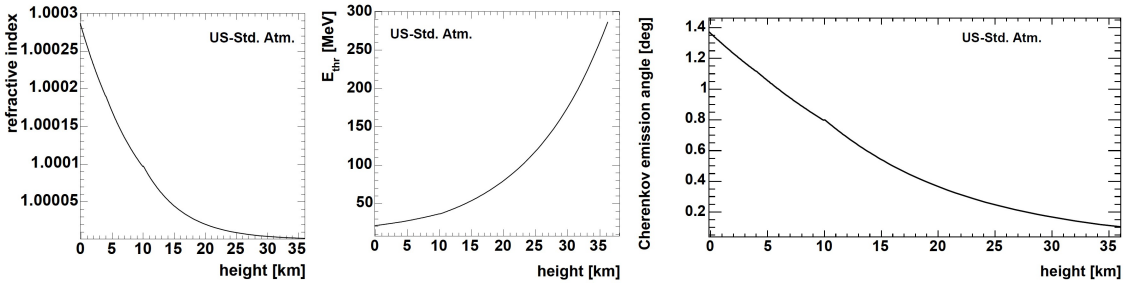

Figure 9: Height dependence with a simplified density dependence for the reference US Standard Atmosphere, without wavelength dependence - Left: for the refractive index n. Middle: for the energy threshold of the Cherenkov emission, simulated for electrons. Right: for the Cherenkov emission angle for an ultra relativistic particle. From [33].

field of view of these telescopes is typically much smaller than that of the fluorescence telescopes, because they are mounted onto a steerable support structure. A positioning system allows for pointing to any source of interest in the sky within seconds, less than a minute. The Cherenkov telescopes are designed to observe the Cherenkov emission typically in the wavelength range between 300 and 600 nm. Because of the similarity of the fluorescence and Cherenkov telescopes, many atmospheric dependences are the same or at least very similar.

Longitudinal shower development and Cherenkov light emission The Cherenkov emission is induced by the charged particles of an EAS developing through the Earth's atmosphere. In addition to the atmospheric dependence of the longitudinal shower development, the atmospheric Cherenkov technique is also sensitive to the refractive index of air n. The number of Cherenkov photons emitted per unit path length of atmospheric depth x can be written as [30]

$$\frac{\mathrm{d}N}{\mathrm{d}x} = 2\pi\alpha z^2 \int_{\lambda_1}^{\lambda_2} \left(1 - \frac{1}{(\beta n(\lambda))^2}\right) \frac{1}{\lambda^2} \mathrm{d}\lambda \tag{4}$$

in the wavelength range λ_1 to λ_2, α being the fine structure constant, z as the charge number, and $\beta = v/c$. The refractive index of air is wavelength-dependent and $n(\lambda) - 1$ changes by about 5% between 300 and 600 nm. One approach to take into account the atmospheric dependences of n is by describing the altitude-dependent variation given by pressure and temperature folded with empirical formulars which describe the wavelength dependence of n for the different components of air as dry air and adjustable fractions of water vapor and CO_2, see [31, 32] and references therein. The altitude-dependent behavior of the refractive index n, the energy threshold for the Cherenkov light emission and its emission angle are shown in Fig. 9, all curves do not include the additional wavelength dependence. The full relevance of the atmospheric dependences for the detection of the Cherenkov emission is demonstrated in a simulation study, shown here for the emission along the shower axis for vertical 100 GeV gamma rays, Fig. 10. In the right panel, the strong variation with different atmospheric conditions becomes evident for photons which are emitted close to the shower core and from below about 10 km. In the next step of the simulation study, the number of Cherenkov photons in the wavelength range of interest is given in a respective field of view of the Cherekov telescope. In the left panel of Fig. 11, the variation of the emitted photons is shown when only the refractive index is calculated for the different atmospheric conditions, but the longitudinal

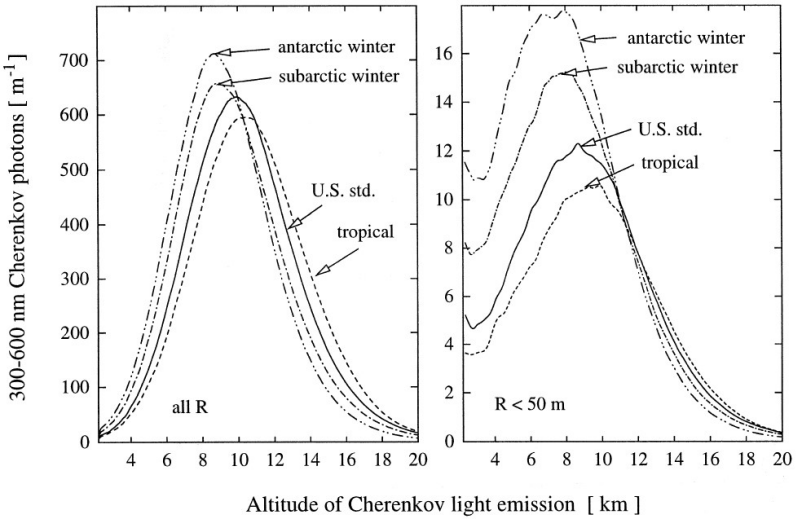

Figure 10: Average Cherenkov light emission along the shower axis for vertical 100 GeV gamma rays with different atmospheric profiles. Left: All emitted photons. Right: Photons which would arrive within 50 m from the core at the observation level of 2200 m. No absorption is applied here. From [30].

development of the shower particles is simulated for the reference US Standard Atmosphere. In the middle and right panels of Fig. 11, the emission is simulated with all atmospheric dependences. The different atmospheric profiles cover all possible sites of gamma ray observatories.

Light transmission towards telescopes The light attenuation for the case of Cherenkov telescopes is the same as for the fluorescence telescopes. The only difference is due to the broader wavelength range of interest and the observation of Cherenkov photons higher up in the atmosphere. For wavelengths longer than about 460 nm, attenuation caused by aerosol scattering becomes dominant over that by molecular scattering. Also the absorption by ozone needs to be considered. The direct transmission of light from space is calculated with MODTRAN and displayed in Fig. 12 [30].

Clouds Clouds in the field of view of Cherenkov telescopes alter the light transmission in the same way as for fluorescence telescopes. Only the observation modus is different for gamma rays. Because of the adaptive scheduling of the observations, the telescopes can be positioned to clear parts of the sky. For Cherenkov telescopes it is typically enough to veto directions in which clouds have been identified by e.g. photometers [35].

2.4 Radio antennas

Since several years, also the radio detection technique is applied for studying EAS induced by ultra-high energy cosmic rays [7]. Typically, the radio telescopes are designed for interferometric observations of the low-frequency radio sky, 10-240 MHz, but with an optimized design the capability to study short, pulsed signals in the time-domain is given [6]. The radio detection of EAS is performed at frequencies between 30 and 80 MHz with an array of several hundred antennas. Current installations record the voltage response of the antennas and the polarization of the electric field. This detection technique is affected by different atmospheric conditions in terms of varying electric fields in the atmosphere. The two main production principles of the radio signals from

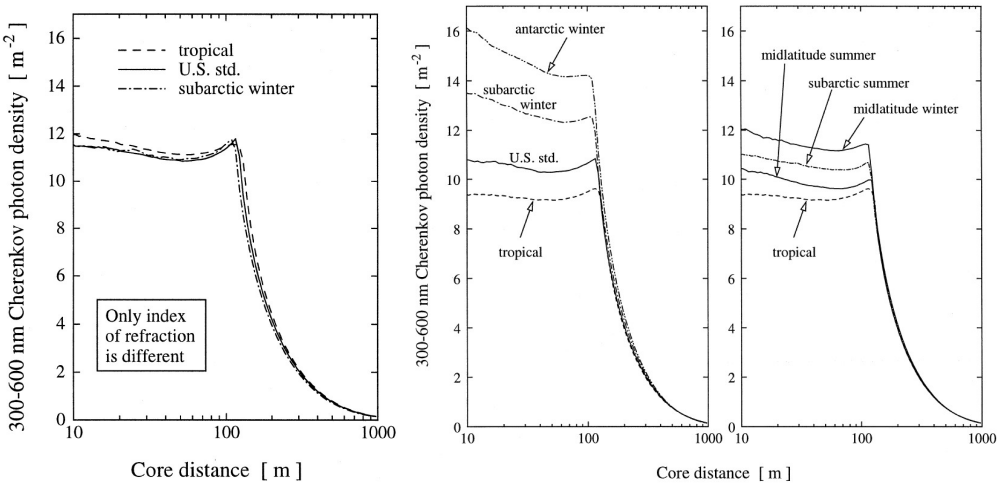

Figure 11: Average lateral distributions of Cherenkov light photons between 300 and 600 nm for vertical 100 GeV gamma rays, given at an observation level of 2200 m above sea level. Absorption of the Cherenkov light is taken into account. Left: Profiles when only the index of refraction is modified according to different atmospheric profiles, but the shower development is in all cases simulated with the reference US Standard Atmosphere. Right: All atmospheric dependences are taken into account, so also the longitudinal development of the showers are simulated with different atmospheric conditions. From [30].

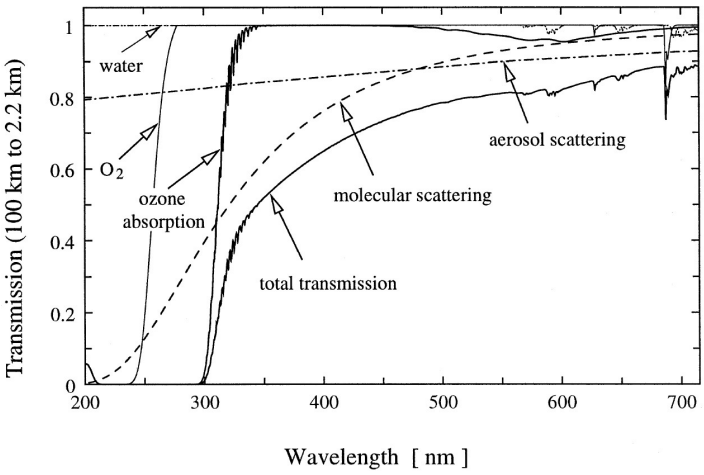

Figure 12: Transmission of light from 100 km to 2.2 km a.s.l. observation level along a vertical path calculated with MODTRAN [34]. From [30].

EAS are illustrated in Fig. 13. Varying strength of the atmospheric electric field alters signals from both production mechanisms of the radio emission. An exemplary profile of an electric field in a thunderstorm condition is shown in Fig. 14. The typical electric field strength in fair weather of few hundred V/m can increase to few hundred kV/m in thunderstorm conditions and, of course, at all altitudes depending on the particlar cloud structure. Different polarization signals of EAS in fair and thunderstorm conditions are displayed in Fig. 15.

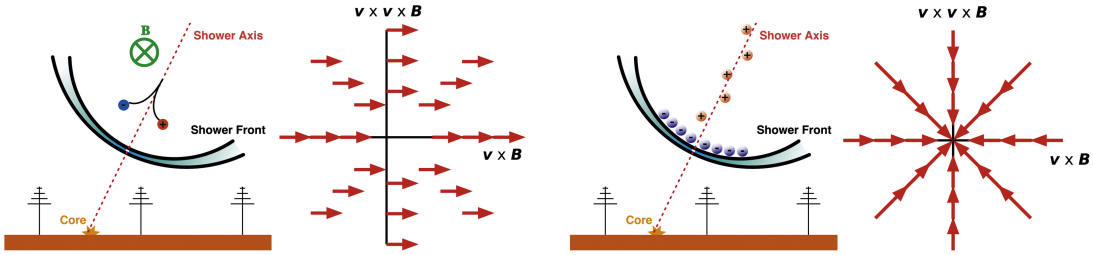

Figure 13: Left: The geomagnetic radiation mechanism. The arrows indicate the direction of linear polarization in the plane perpendicular to the EAS axis. Right: The charge excess (Askaryan) emission. The polarization is linear with electric field vectors oriented radially to the shower axis. From [36].

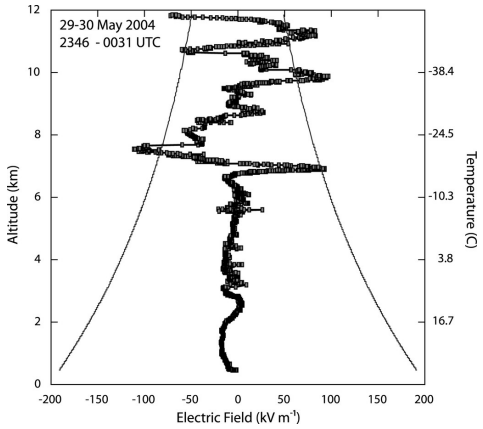

Figure 14: Electric field sounding through a high-precipitation tornadic supercell storm in Oklahoma on 29 May 2004 and breakeven electric field (solid thin lines) as calculated in that reference. Individual measurements of electric field values are noted as small squares along sounding trace. Temperature is taken from the same sounding, shown every 2 km on the right y axis. The weather balloon was launched at 23:46 UTC and reached maximum altitude of 11.8 km at 00:31 UTC, corresponding to 18:46 and 19:31 local time, respectively. From [37], © American Meteorological Society. Used with permission.

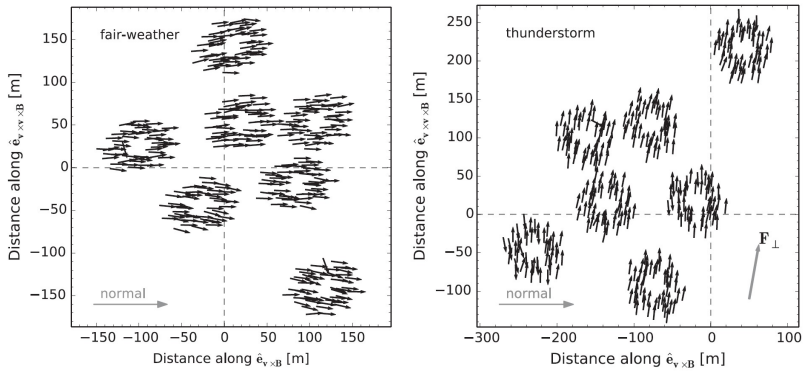

Figure 15: Polarization as measured with individual LOFAR antennas (arrows) in the shower plane of measured air showers. LOFAR antennas are grouped into circular stations, of which seven are depicted. The expected polarization direction for fair-weather air showers is indicated with "normal". The position of the shower axis, orthogonal to the shower plane, is indicated by the intersection of the dashed lines. Left: Fair-weather conditions. Right: Thunderstorm conditions. From [38].

3. Instruments for Atmospheric Monitoring

The different aspects of atmospheric conditions, which are relevant for the astroparticle physics observations, can be grouped in five categories. Several atmospheric monitoring devices are used for the different categories or an instrument can serve in more categories. The **first category** is related to the so-called molecular part of the atmosphere, as the state variables are of interest together with derived information like atmospheric depth, refractive index, and Rayleigh scattering. The standard instrument for recording those data at ground are weather stations. Profiles of state variables can be obtained by meteorological radio soundings or data from global atmospheric models provided by many large meteorological organizations can be used. Some information about state variables can also be retrieved from Raman lidars. The **second category** is about the scattering of light at aerosols, the Mie scattering. Instruments for measuring the actual Mie scattering at an observatory are elastic lidars, bistatic elastic lidars which are also called laser facilities, Raman lidars, FRAM - ph(F)otometric Robotic Atmospheric Monitor, and photometers. Some of these devices provide altitude-dependent information while others provide an overall optical transmission through the entire atmosphere. The **third category** is the detection of clouds and all instruments for the aerosol scattering are also used for cloud detection. Furthermore, infrared cloud cameras can observe the atmosphere to detect clouds, and there are also some satellites that provide different sky temperatures which can be used to identify cloud. Some of the satellite data are publicly available from the large meteorological organizations. The **fourth category** is the observation of the electric field in the atmosphere and of lightning. The field strength can be measured with electric field mills. Lightning strokes can also be mapped with special high-speed video cameras, or even the radio antennas mentioned above can be used. The **fifth category** covers so-called slow control systems of the observatories and is necessary for the safe operation of the observatory detectors. Here weather stations, wind sensors, electric field mills, or dust monitors are in use.

At all observatories in high-energy astroparticle physics many different atmospheric monitoring devices are installed providing those information needed for the particular purposes. In this review, it is not possible to detail all the different sets of instruments, so only few are mentioned here exemplarily. Over the years, a small community has formed that is discussing the different monitoring techniques and applications in a series of workshops. The presentations of these workshops are publicly available and for some proceedings have been published. The first of these workshops took place in Paris in May 2003 as the "Astroparticle and Atmosphere (AA) workshop" [39]. The second and third workshops held the label ATMON - Atmospheric Monitoring in Astroparticle Physics and Astronomy, and were held in Prague in 2008 [40] and in Wisconsin in 2010 [41]. Since 2013, the workshop series holds the label AtmoHEAD - Atmospheric Monitoring for High-Energy AstroParticle Detectors. In 2013, the meeting was in Paris-Saclay [42]. For the workshops in Padova in 2014 [43], in Olomouc in 2016 [44], in Anacapri in 2018 [45] and in 2022 [46], proceedings have been published for each workshop, see for AtmoHEAD2014 [47], AtmoHEAD2016 [48], AtmoHEAD2018 [49], and for AtmoHEAD2022 [50].

First category Many details about the different suits of atmospheric monitoring devices are given at those workshops and an illustration of such a composition is shown in Fig. 16 for the Pierre Auger Observatory. Data of atmospheric state variables are recorded by several weather stations

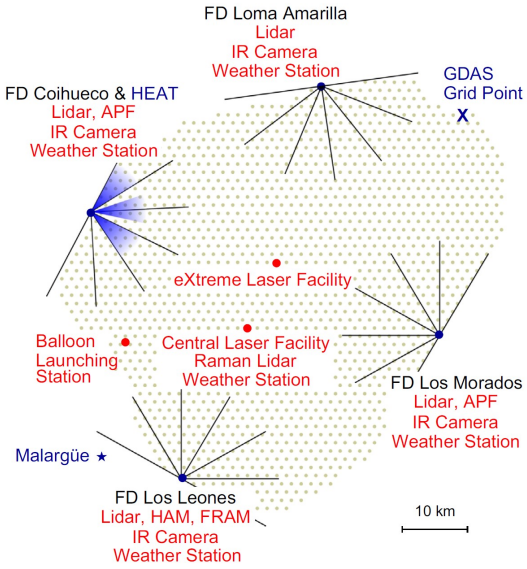

Figure 16: Schematic overview of the atmospheric monitoring devices installed at the Pierre Auger Observatory. The four sites of the Fluorescence Detector are labeled as FD plus its name with lines indicating the horizontal width of the field of view of each telescope and the grid of particle detectors at ground is marked by a small grey dot for each Surface Detector water-Cherenkov tank. From [4].

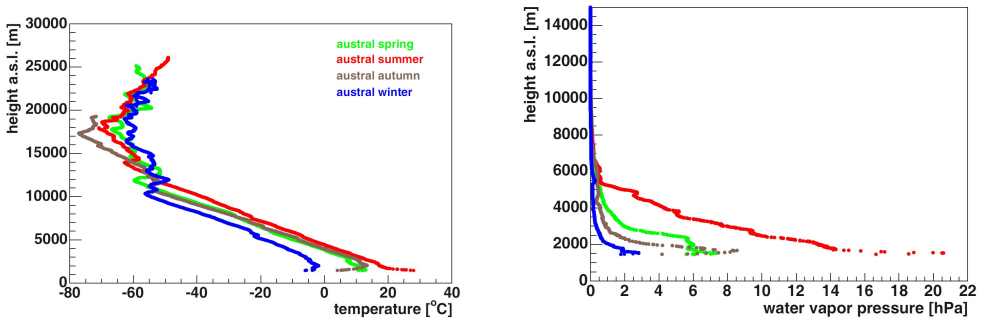

Figure 17: One exemplary atmospheric profile per season obtained by meteorological radiosondes above the array of the Pierre Auger Observatory. Left: Temperature. Right: Water vapor pressure. From [51].

distributed over the array. Between 2002 and 2010 intermittent launches of weather balloons were performed additionally [51]. Overall, 331 atmospheric profiles could be recorded whereof 52 were part of a dedicated campaign, called rapid atmospheric monitoring program, when particularly high-energy EAS detected by the Fluorescence Detector triggered the start of a meteorological radio sounding [52]. The atmospheric profiles were measured typically up to above 20 km a.s.l., but mostly only the lowest about 8 km were above the area of the observatory. Examples of temperature and humidity profiles during different seasons are displayed in Fig. 17. For the temperature, inversion layers close to ground can be seen in these examples for autumn and winter, and mainly during summer conditions, the absolute water content close to ground is of significance. Since launching of radiosondes is quite laborious, in particular at quite remote places as those of the observatories in astroparticle physics, it is desirable to replace local measurements with suitable

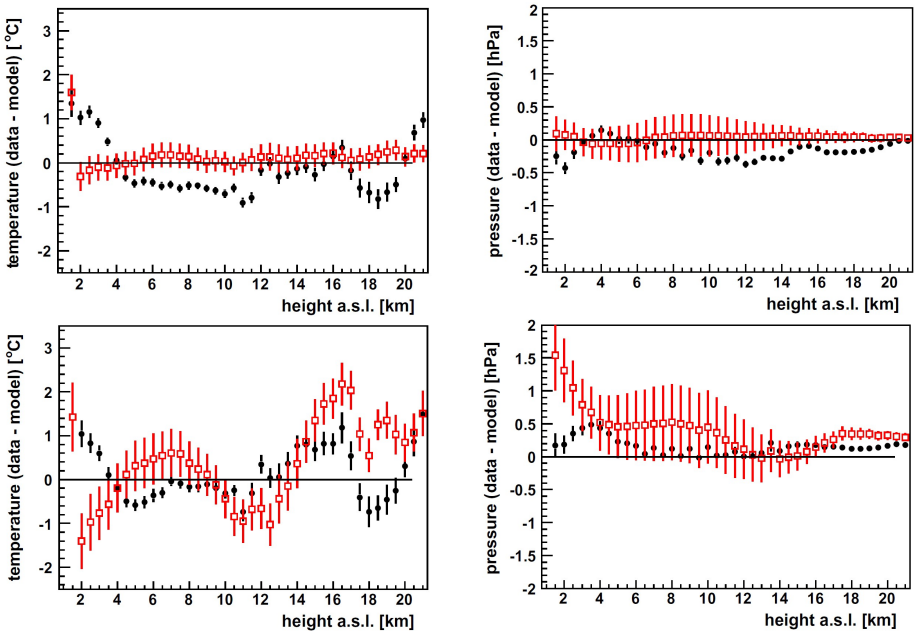

Figure 18: Difference of measured data and GDAS models (black dots) and monthly mean profiles (red squares) versus height. The upper panels show data for temperature and pressure for all radio soundings between 2005 and 2008 and the corresponding 3-hourly GDAS profiles. The monthly mean profiles were built from this local data set. The lower panels show radio soundings performed in 2009 and 2010. From [53].

data provided by e.g. meteorological organizations or by e.g. monthly models [53, 54]. The Global Data Assimilation System (GDAS) is such an atmospheric model developed at NOAA's National Centers for Environmental Prediction and it provides 3-hourly data at 23 constant pressure levels on a global 1°-spaced latitude-longitude grid [55]. In a study for the Auger Observatory, local measurements, derived monthly models, and GDAS profiles have been compared to evaluate the validity of model data for that site, see Fig. 18. It can be seen that the uncertainty for monthly models is larger than for the 3-hourly GDAS profiles, in particular for periods which were not considered for building those monthly models (lower panels in Fig. 18). The validity of corresponding GDAS data for an adequate accuracy with respect to horizontal and vertical as well as temporal resolution could be confirmed. Compared to monthly models, the resulting reconstruction uncertainty for the energy and $X_{\max}$ of EAS caused by atmospheric variances is halved [53].

For other observatories, like the IceCube neutrino observatory, the use of global model data for atmospheric conditions is even more mandatory. Neutrinos, which are detected in the IceCube detector in the ice at the South pole, are produced by meson decays in cosmic-ray-induced air showers that developed in the Earth's atmosphere all around the globe, see Fig. 19, left. Based on more than 260 000 neutrino events, the significant ($> 10\sigma$) observation of a correlation between the rate of neutrino events and atmospheric temperatures of the stratosphere is reported [56]. For the observed 10% seasonal change of the effective atmospheric termperature, a correlation of 4.3% has been expected from theoretical predictions under the assumption of various hadronic interaction models. However a 3.5% change in the muon neutrino flux is measured, giving a deviation of about 2-3 standard deviations from the expectation. A re-analysis of systematically selected subsets of the

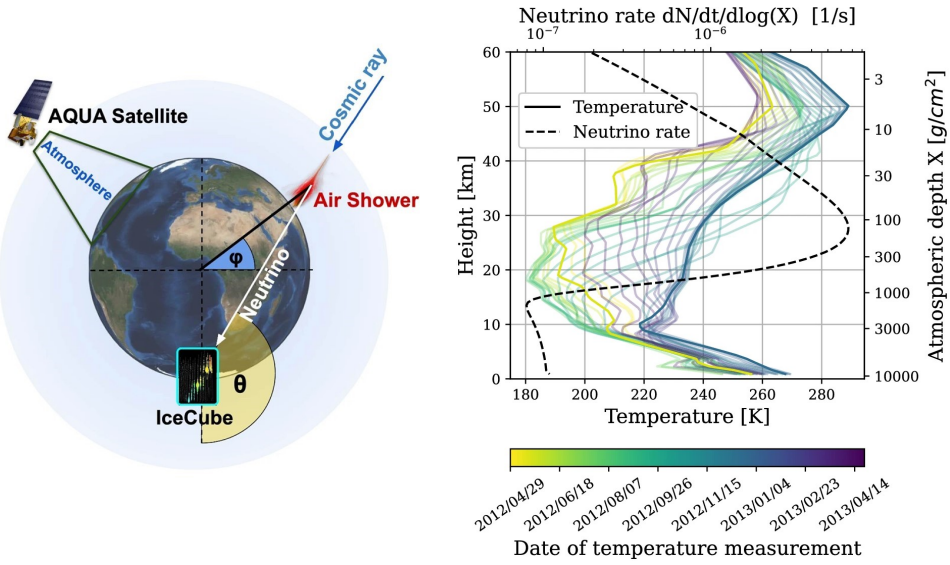

Figure 19: Left: Sketch of the experimental setup. In the right half, the production, propagation and measurement of an atmospheric ν_μ with IceCube is shown. In the top left, the measurement of the temperature by the AIRS instrument is illustrated. Right: Example of altitude-profiles of atmospheric temperatures between 2012 and 2013 for some experimental conditions. The dashed black line represents the average effective production-profile of atmospheric ν_μ. The small rise towards lower atltitude is not related to meson decays but to muon decays in flight. From [56].

data shows deviations from the average model, with some being predicted (reconstructed energy) and others not being predicted (rising/falling temperature, extreme temperatures), see Fig. 20. This result shows that a thorough understanding of atmospheric conditions is essential for high-level analyses of astroparticle physics data. Uncertainties induced by atmospheric effects might hinder the understanding of e.g. hadronic interactions in air shower development.

Second and third category Elastic lidars are widely used for monitoring the aerosol scattering and clouds at astroparticle physics observatories. A strong laser signal is shot into the atmosphere and the backscatter signal is received by a small optics in the lidar installation. Because of the strong light pulse, these measurements interfer with astroparticle physics observations. For the large field of view of fluorescence telescopes and their continuous data taking during dark nights with only minor moon illumination, intensive usage of lidars would cause severe loss of observation time. In case of Cherenkov telescopes, lidars can be used to observe the atmospheric conditions close to the field of view of the Cherenkov telescopes, providing adequate atmospheric information without interfering the main observations of the observatory. At the MAGIC observatory for detecting gamma rays, an elastic lidar is operated quasi-continuously during MAGIC data taking since 2015 [57]. The lidar follows the MAGIC telescope tracking direction within $\sim 5°$ distance. A data correction using the atmospheric transmission profiles has been developed recently. In Fig. 21, the performance of this correction is demonstrated. A new approach for applying such atmospheric corrections to Cherenkov telescope data without dedicated local measurements is currently being investigated and first results are presented at this conference [58]. An update on lidar observations at the Auger Observatory is also given at this conference [59].

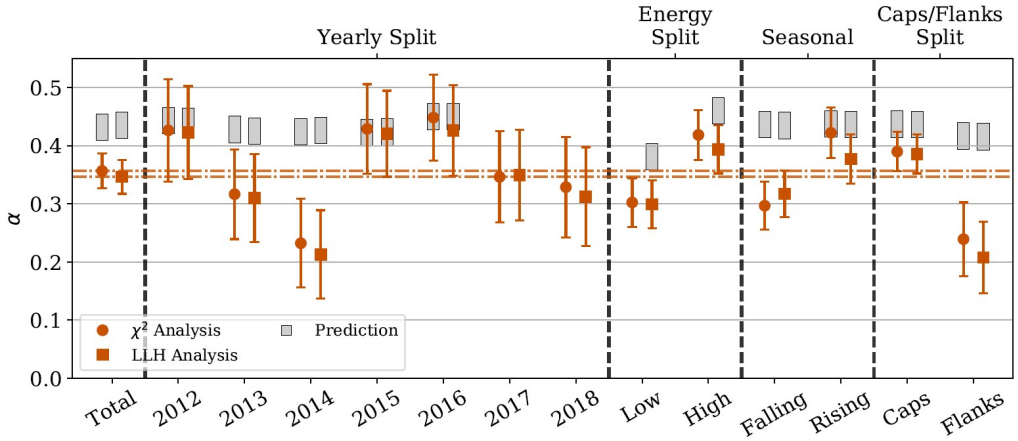

Figure 20: Plot summarizing the main results for the slope parameter α, being the strength of the correlation between the atmospheric temperatures and the measured atmospheric ν_μ rates. The different re-analyses are marked by dots and squares while the predictions of the respective data are shown as grey bands including uncertainties. The dashed horizontal line is the overall result for α. Frrom [56].

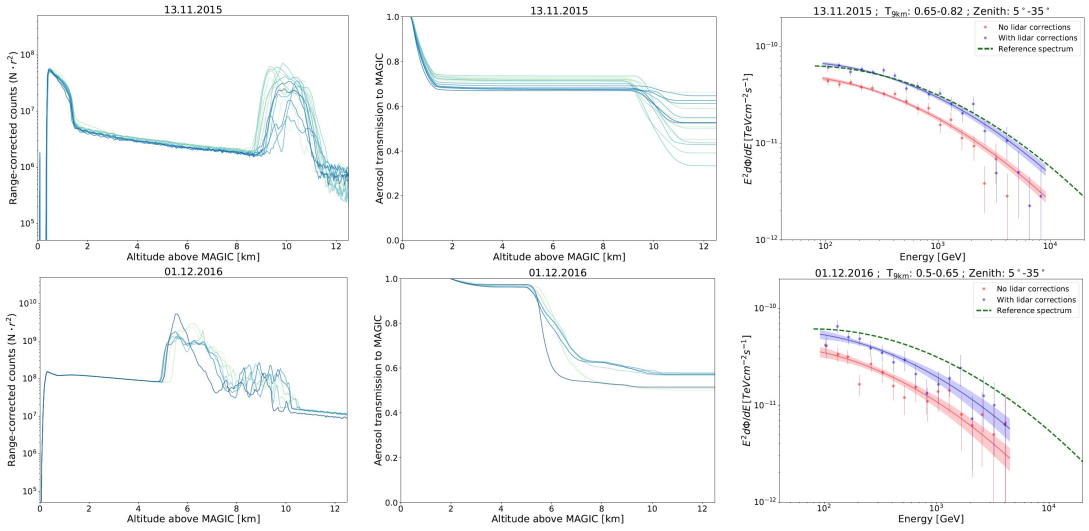

Figure 21: The left panels show the lidar profiles as range-corrected photo-electron counts and the middle panels are the resulting integral aerosol transmission curves. In the right panels, the reconstructed spectral energy distributions of the concurrent observations of the Crab Nebula are shown, in red without and in blue with lidar correction. The upper example is for favorable conditions where a structured cloud layer is detected between about 9 to 11 km, and the lower example depicts unfavorable conditions with strong cloud interference at a broad range in altitude. From [57].

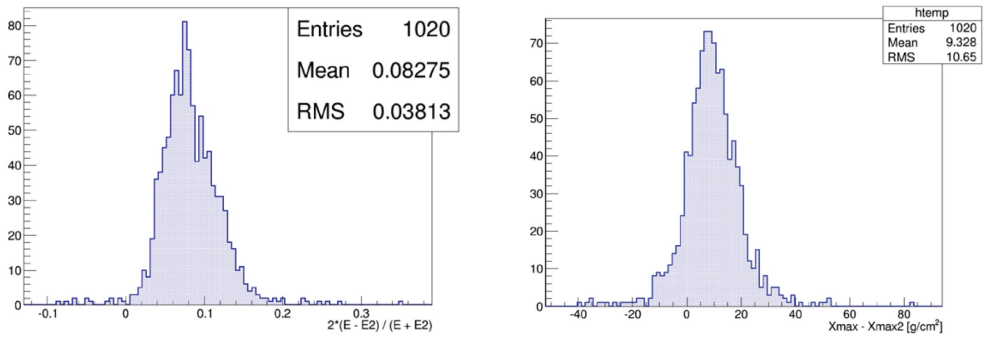

Figure 22: Distribution of reconstructed EAS parameter using mean VAOD of 0.04 vs. 0.02 in a parametric model, including the variance of actual optical properties. Left: Energy. Right: $X_{\max}$. From [28].

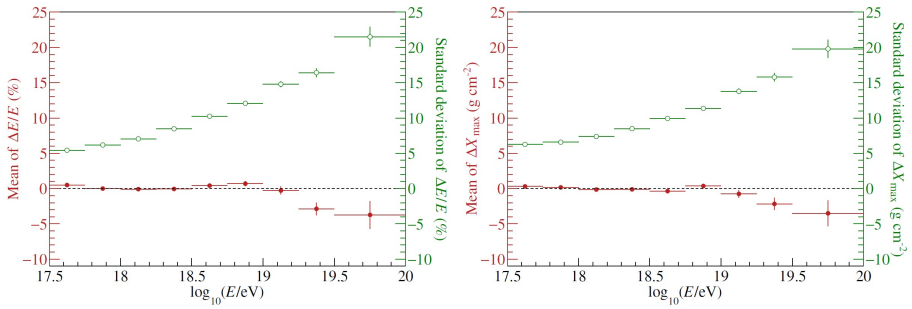

Figure 23: EAS reconstruction using an average aerosol profile minus those from hourly aerosol profiles. Filled red circles plot the mean of the distribution in each energy bin, and open green circles plot the standard deviation. Left: Energy of EAS. Right: Position of shower maximum. From [60].

At observatories using fluorescence telescopes also bi-static elastic lidars are used. A strong laser signal is shot into the atmosphere from a central position at the array of the observatory and the sidescattered signal is detected with the fluorescence telescopes themselves. Mean values for the vertical aerosol optical depth VAOD in a parametric model, including the variance of acutal optical properties, are used for studying the systematic uncertainty and the resolution of the reconstructed EAS parameters energy and $X_{\max}$ for Telescope Array. In Fig. 22, the pull for these two parameters is shown if the typically applied mean VAOD of 0.04 is changed to very clear conditions of VAOD of 0.02. The energy is shifted by more than 8% with a resolution of about 4%, and for the position of the EAS maximum the shift is almost 10 g/cm^2 with a resolution of about 11 g/cm^2. Applying hourly aerosol information improves the resolution of the EAS reconstruction compared with average aerosol profiles as studied for the Pierre Auger Observatory [60], see Fig. 23. Further improvements of this implementation of aerosol data in the EAS reconstruction are presented at this conference [61].

With a ph(F)otometric Robotic Atmospheric Monitor, FRAM, the overall atmospheric optical depth can be derived. A CCD camera with a photographic lens on an equatorial mount provides wide-field images of stars which can be compared to their cataloged brightness [62, 63]. This passive method does not inferfer with any other observation technique and is used for characterizing the conditions at possible observatory sites, for example, see Fig. 24.

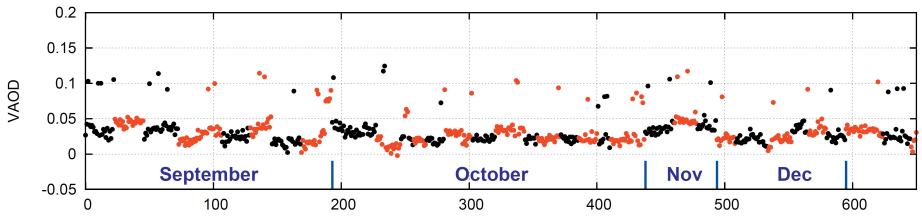

Figure 24: Time series of VAOD measurements taken by the CTA FRAM telescope located near Cerro Paranal in Chile in 2017. From [64].

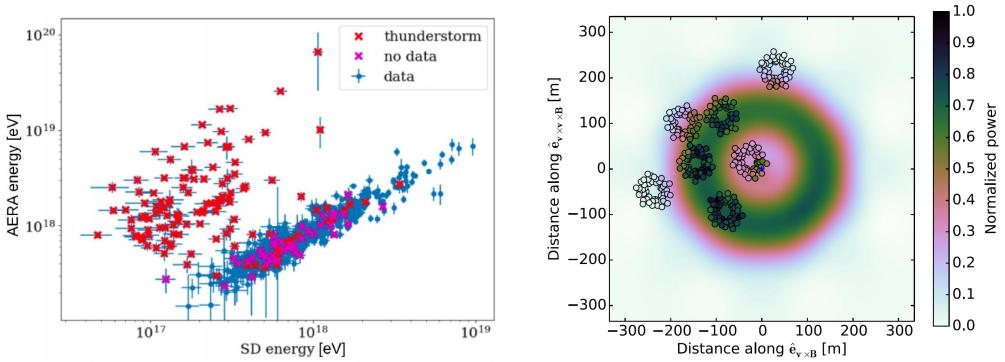

Figure 25: Left: Reconstructed EAS energy from the AERA radio detectors at the Auger Observatory vs. the energy obtained by the particle detector at ground. Data for fair weather conditions are marked as blue crosses, and EAS events recorded during thunderstorm conditions are indicated by red asterisk. Adapted from [65]. Right: Radio intensity pattern during a thunderstorm. The circles represent antenna positions from LOFAR. Their color reflects measrued pulse power. The best-fitting simulation is shown in color scale in the background. Where the colors of the circles match the background, a good fit is achieved. From [38].

Fourth category Electric field mills measure the conditions at ground. For current radio detectors, the E-field data can be used to identify bad weather conditions when the radio signals are affected. In Fig. 25, left, it can be seen that the good correlation between reconstructed energy of EAS measured by radio antennas and by particle detectors at ground is broken for thunderstorm conditions [65]. Applying simple two-layer models for the atmospheric electric field, it is even possible to reproduce antenna signal patterns by state-of-the-art simulation codes [38], see Fig. 25, right.

4. Interdisciplinary Spin-offs

Atmospheric monitoring at astroparticle physics observatories uses many techniques from meteorology and climatology. An interdisciplinary character of this field is naturally given. From the many cooperations and common topics, several advanced interdisciplinary spin-offs have evolved over the years.

Lightning mapping A fundamental understanding of lightning is still missing, in particular the initiation and early development of a lightning flash remain unknown. With the LOFRAR antenna array, lightnings are studied in great detail and the stages of a lightning flash are imaged [66]. In Fig. 26, the four dimensional mapping of a lightning flash is illustrated. In a recent work, the antenna signals are interpreted to understand the inital breakdown pulse [67], Fig. 27.

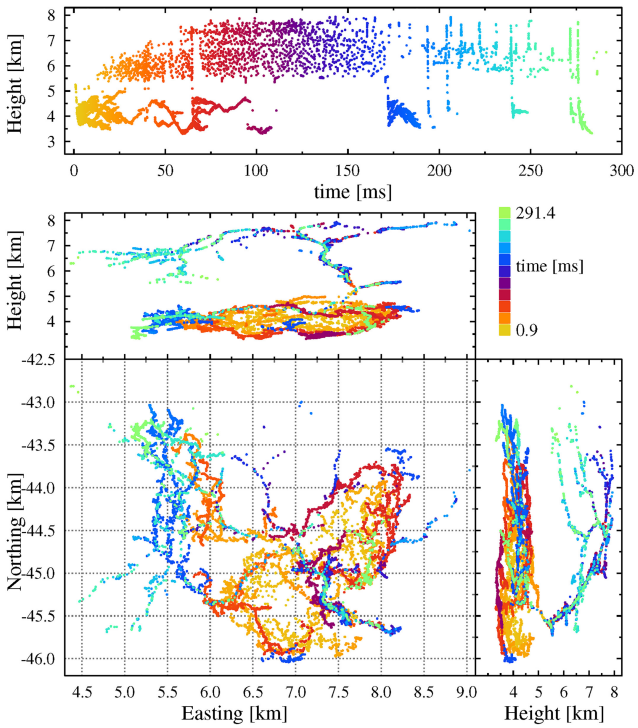

Figure 26: Image of a lightning flash recorded at LOFAR in 2018. The top panel shows height vs. time of the sources where an offset to put initation close to $t = 0$ is applied. The same sources, with the same coloring, are shown in the other panels giving height and distances north and east from the LOFAR core. From [66].

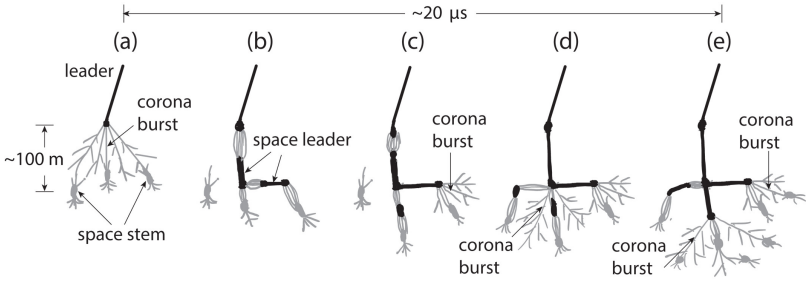

Figure 27: Diagram of the initial breakdown pulse generation process. (a) Multiple space stems appear from the initial corona burst. (b) Two space leaders are formed, each connecting to a space stem downstream. (c) The junction of the two space leaders creates a corona burst, as well as a brief current pulse. (d) The connection between the space leader with the main leader sets off an intense corona burst. (e) Connection between a space leader further downstream with the main leader. Black and gray colors represent hot (i.e., leaders) and cold (e.g., streamers) plasma channels/structures, respectively. A corona burst is a burst of VHF emitting streamers; a space stem is a cold plasma structure that extends bidirectionally through forward propagating negative streamers and backward propagating positive streamers; and a space leader is formed when the temperature of a space stem is sufficiently high to maintain its conductivity. From [67].

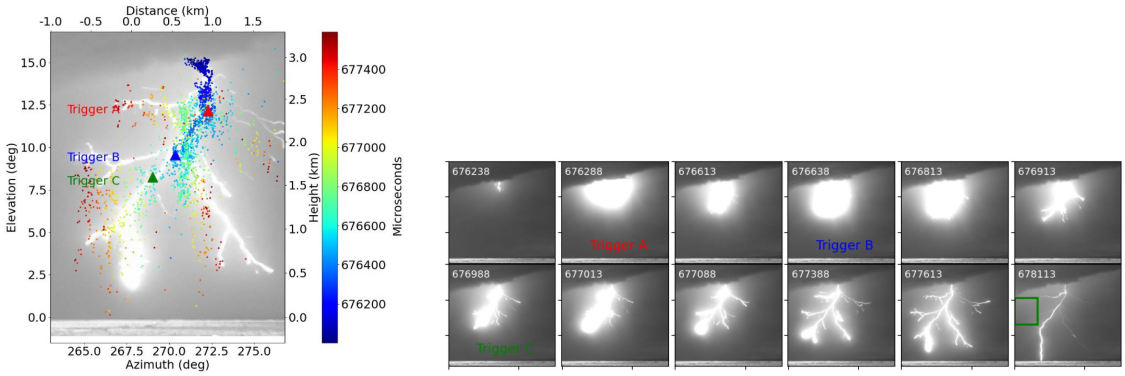

Figure 28: Terrestrial Gamma Ray Flash detected at Telescope Array with a high-speed video camera. Left: Elevation vs. azimuth for the whole flash. Right: Sequence of 12 images selected to cover the view of the whole flash. The time differences between the images does not corresond to the time resolution of the camera. From [69].

Terrestrial Gamma Ray Flashes Terrestrial Gamma Ray Flashes (TGF) were reported for the first time in 1994 based on satellite data. TGF are produced by lightning flashes and early observations indicate that the TGF stem from upward intracloud flashes. Later observations by ground experiments confirmed that TGF can also be detected at ground level. The surface detector of Telescope Array has also recorded such TGF during lightning [68]. Recent studies present that those TGF detected at ground are produced in a different mechanism, namely by the downward negative breakdown that occurs at the beginning of negative cloud-to-ground flashes. Together with a dedicated Lightning Mapping Array and high-speed video cameras, TGF are investigated further at Telescope Array [69]. An image of a TGF is presented in Fig. 28. Updates of these studies are presented at this conference [70].

Emission of Light and Very Low Frequency perturbations due to Electromagnetic pulse Sources ELVES are a class of transient luminous events in the lower ionosphere spanning over distances of more than 250 km which occur above strong electrical storms. First observations were reported in the 1990s. Records of ELVES events in the data of the fluorescence telescopes of the Pierre Auger Observatory were found from the beginning of its data taking [71]. In 2014, the readout and trigger system was adjusted for better identification of ELVES signatures. Until 2020, the Auger Observatory recorded more than 1 500 events, see Fig. 29. Advanced studies of ELVES with the Auger Observatory are presented at this conference. [72].

Measurements of the laser of the Aeolus satellite The wind mission Aeolus of the European Space Agency operated a space-borne lidar instrument onboard the Aeolus satellite between 2018 and 2023. In a novel cooperation of this ESA team and the Pierre Auger Observatory, benefits for both partners could be achieved [73]. Records of the laser track across the Auger array taken with the fluorescence detector improved the positioning reconstruction of the satellite system, Fig. 30. Further analyses of the laser tracks and possible following satellite missions will be used to provide an additional energy calibration for the Auger Observatory and studies of optical conditions at the experimental site.

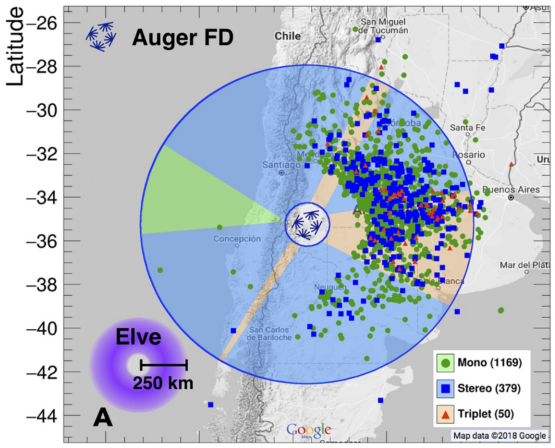

Figure 29: Map denoting the location of the reconstructed lightning strikes causing ELVES seen by the Auger Observatory, in geodetic coordinates. The large and small circles outline the lower and upper boundaries of the pixel array when projected to the base of the ionosphere. The lightning strike location from the detected ELVES and the number of sites of the fluorescence detector contributing to each observation are given. The overlap of the field of view of each detector sites is shown in the shaded regions. From [71].

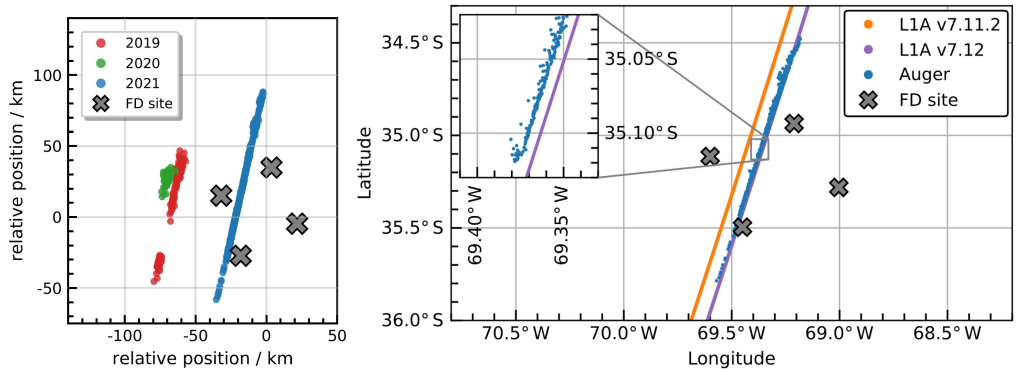

Figure 30: Left: Measured ground tracks for three sample Aeolus overpasses over the Pierre Auger Observatory in the years 2019, 2020, and 2021. The sites of the fluorescence detector are indidated as grey crosses. Right: Comparison between the geolocation derived with different Aeolus data processor versions before (orange line) and after (purple line) the fix of an error together with the measurements by the Auger Observatory (blue dots). From [73].

Acknowledgements

B.K. acknowledges the support of the colleagues from MAGIC, CTA, H.E.S.S., LOFAR, IceCube, TA, and Pierre Auger Observatory to collect the presented information and results.

References

[1] B Keilhauer *EPJ Web Conf.* **197** (2019) 02001.
[2] T. Abu-Zayyad *et al.*, Telescope Array Collaboration *NIM A* **689** (2012) 87–97.
[3] R. Abbasi *et al.*, IceCube Collaboration *NIM A* **700** (2013) 188–220.
[4] A. Aab *et al.*, Pierre Auger Collaboration *NIM A* **798** (2015) 172–213, arXiv:1502.01323v5 [astro-ph.HE].

[5] H. Tokuno *et al.*, Telescope Array Collaboration *NIM A* **676** (2012) 54–65.

[6] P Schellart *et al.*, LOFAR Collaboration *A&A* **560** (2013) A98.

[7] P. Abreu *et al.*, Pierre Auger Collaboration *Journal of Instrumentation* **7** no. 10, (Oct, 2012) P10011.

[8] K. Bernlöhr *et al.*, H.E.S.S. Collaboration *Astroparticle Physics* **20** no. 2, (2003) 111–128.

[9] D. Ferenc, MAGIC Collaboration *NIM A* **553** no. 1, (2005) 274–281. Proc. of the fifth International Workshop on Ring Imaging Detectors.

[10] M. Actis *et al.*, CTA Consortium Collaboration *Experimental Astronomy* **32** (2011) 193–316.

[11] J. Adams *et al.*, JEM-EUSO Collaboration *Space Science Reviews* **218** no. 1, (2022) 3.

[12] A. Olinto *et al.*, POEMMA Collaboration *Journal of Cosmology and Astroparticle Physics* **06** (2021) 007.

[13] J. Abraham *et al.*, Pierre Auger Collaboration *Astroparticle Physics* **32** no. 2, (2009) 89–99, arXiv:0906.5497 [astro-ph.HE].

[14] B. Keilhauer. PhD thesis, Forschungszentrum Karlsruhe, 2004. https://publikationen.bibliothek.kit.edu/4512003/3868239.

[15] B. Keilhauer *et al. Astroparticle Physics* **22** no. 3, (2004) 249–261, arXiv:0405048v2 [astro-ph.HE].

[16] A. N. Bunner. PhD thesis, Cornell University, 1967. https://inspirehep.net/literature/1087629.

[17] F. Arqueros, J. R. Hörandel, and B. Keilhauer *NIM A* **597** no. 1, (2008) 1–22. Proc. of the 5th Fluorescence Workshop.

[18] M. Ave *et al.*, AIRFLY Collaboration *NIM A* **597** no. 1, (2008) 50–54. Proc. of the 5th Fluorescence Workshop.

[19] B Keilhauer *et al. EPJ Web Conf.* **53** (2013) 01010, arXiv:1210.1319v2 [astro-ph.HE].

[20] F. Arqueros, J. R. Hörandel, and B. Keilhauer *NIM A* **597** no. 1, (2008) 23–31. Proc. of the 5th Fluorescence Workshop.

[21] J. Rosado, F. Blanco, and F. Arqueros *Astroparticle Physics* **55** (2014) 51–62, arXiv:1401.4310 [astro-ph.HE].

[22] M. Ave *et al.*, AIRFLY Collaboration *NIM A* **597** no. 1, (2008) 41–45. Proc. of the 5th Fluorescence Workshop.

[23] Y. Tsunesada *et al.* in *33rd International Cosmic Ray Conference*, p. 1014. 2013. https://inspirehep.net/files/03868d77284f6387f31a188982b07654.

[24] B. Keilhauer *et al. NIM A* **597** no. 1, (2008) 99–104. Proc. of the 5th Fluorescence Workshop.

[25] J. Abraham *et al.*, Pierre Auger Collaboration *Astroparticle Physics* **33** no. 2, (2010) 108–129, arXiv:1002.0366 [astro-ph.HE].

[26] T. Tomida *et al. EPJ Web Conf.* **53** (2013) 10003.

[27] B.R. Dawson *EPJ Web Conf.* **197** (2019) 01004.

[28] T. AbuZayyad *EPJ Web Conf.* **197** (2019) 01003.

[29] K. Louedec, Pierre Auger Collaboration in *32nd International Cosmic Ray Conference*. 8, 2011. https://doi.org/10.48550/arXiv.1107.4806.

[30] K. Bernlöhr *Astroparticle Physics* **12** no. 4, (2000) 255–268.

[31] J. C. Owens *Appl. Opt.* **6** no. 1, (Jan, 1967) 51–59.

[32] B.A. Bodhaine *et al. J Atmospheric Oceanic Technology* **16** no. 11, (1999) 1854.

[33] F. Nerling. PhD thesis, Universität Karlsruhe (TH), 2005. https://publikationen.bibliothek.kit.edu/1000002956.

[34] F. Kneizys *et al.* Tech. Rep. 1731-3010, Phillips Laboratory, Geophysics Directorate, PL/GPOS, 29 Randolph Road, 01, 1996. https://web.gps.caltech.edu/~vijay/pdf/modrept.pdf.

[35] M. Will *EPJ Web Conf.* **144** (2017) 01002.

[36] T. Huege *NIM A* **876** (2017) 9–12. The 9th international workshop on Ring Imaging Cherenkov Detectors (RICH2016).

[37] K. M. Calhoun *et al. Monthly Weather Review* **141** no. 7, (2013) 2199 – 2223.

[38] P. Schellart *et al. Phys. Rev. Lett.* **114** (Apr, 2015) 165001.

[39] J. B. Gordo, Y. Gallant, E. Parizot, and E. Plagnol, "Astroparticle and Atmosphere (AA) workshop," May, 2003. hess.in2p3.fr/aaa.

[40] M. Prouza *et al.*, "Atmospheric Monitoring for Astroparticle Physics - ATMON08 workshop," Jun, 2008. www.particle.cz/ATMON08.

[41] S. BenZvi *et al.*, "Workshop on Atmospheric Monitoring in Astroparticle Physics and Astronomy - ATMON'10," Sep, 2010. https://events.icecube.wisc.edu/event/30/timetable/?print=1&view=standard_inline_minutes.

[42] R. Chaves *et al.*, "AtmoHEAD: Atmospheric Monitoring for High-Energy Astroparticle Detectors," Jun, 2013. https://indico.in2p3.fr/event/7898/.

[43] M. Doro *et al.*, "AtmoHEAD 2014: Atmospheric Monitoring for High-Energy Astroparticle Detectors," Mai, 2014. https://agenda.infn.it/event/6911/.

[44] D. Mandat *et al.*, "AtmoHEAD 2016," Sep, 2016. http://jointlab.upol.cz/cta/ATMOHEAD/index.php.

[45] L. Valore *et al.*, "AtmoHEAD 2018," Sep, 2018. https://agenda.infn.it/event/14467/.

[46] L. Valore *et al.*, "AtmoHEAD 2022," Jul, 2022. https://agenda.infn.it/event/30210/.

[47] M. Doro, ed., *AtmoHEAD 2014: Atmospheric Monitoring for High Energy AstroParticle Detectors*, vol. 89. EPJ Web of Conferences, 2015. https://www.epj-conferences.org/articles/epjconf/abs/2015/08/contents/contents.html.

[48] P. Travnicek, M. Prouza, M. Gaug, and B. Keilhauer, eds., *Atmospheric Monitoring for High Energy Astroparticle Detectors (AtmoHEAD) 2016*, vol. 144. EPJ Web of Conferences, 2017. https://www.epj-conferences.org/articles/epjconf/abs/2017/13/contents/contents.html.

[49] L. Valore, R. Colalillo, and F. Guarino, eds., *Atmospheric Monitoring for High Energy Astroparticle Detectors (AtmoHEAD) 2018*, vol. 197. EPJ Web of Conferences, 2019. https://www.epj-conferences.org/articles/epjconf/abs/2019/02/contents/contents.html.

[50] C. Aramo, R. Colalillo, F. Guarino, and L. Valore, eds., *Atmospheric Monitoring for High Energy Astroparticle Detectors 2022 (AtmoHEAD 2022)*, vol. 2398. Journal of Physics: Conference Series, 2022. https://iopscience.iop.org/issue/1742-6596/2398/1.

[51] B. Keilhauer and M. Will, Pierre Auger Collaboration *EPJ plus* **127** (2012) 96.

[52] P. Abreu *et al.*, Pierre Auger Collaboration *Journal of Instrumentation* **7** no. 09, (Sep, 2012) P09001.

[53] P. Abreu *et al.*, Pierre Auger Collaboration *Astroparticle Physics* **35** no. 9, (2012) 591–607, arXiv:1201.2276 [astro-ph.HE].

[54] R. Abbasi *et al.*, Telescope Array Collaboration *Astroparticle Physics* **80** (2016) 131–140.

[55] Environmental Modeling Center, National Centers for Environmental Prediction, National Weather Service, NOAA, U.S. Department of Commerce, "Global Data Assimilation System (GDAS1) Archive Information." https://www.ready.noaa.gov/gdas1.php.

[56] R. Abbasi *et al.*, IceCube Collaboration *EPJ C* **83** (2023) 777.

[57] F. Schmuckermaier *et al. A&A* **673** (2023) A2.

[58] T. L. Holch *PoS* **ICRC2023** (2023) 779.

[59] J. Rodriguez *et al.*, Pierre Auger Collaboration *PoS* **ICRC2023** (2023) 374.

[60] V. M. Harvey, Pierre Auger Collaboration *PoS* **ICRC2019** (2019) 283.

[61] V. M. Harvey *et al.*, Pierre Auger Collaboration *PoS* **ICRC2023** (2023) 300.

[62] J. Ebr *et al. The Astronomical Journal* **162** no. 1, (Jun, 2021) 6.

[63] A. Aab *et al.*, Pierre Auger Collaboration *Journal of Instrumentation* **16** no. 06, (Jun, 2021) P06027.

[64] P. Janecek *et al. EPJ Web Conf.* **197** (2019) 02008.

[65] M. Gottowik. PhD thesis, Bergische Universität Wuppertal, 2021. https://elekpub.bib.uni-wuppertal.de/urn/urn:nbn:de:hbz:468-20210825-115231-6.

[66] O. Scholten *et al. Journal of Geophysical Research: Atmospheres* **126** no. 4, (2021) e2020JD033126.

[67] N. Y. Liu *et al. Geophysical Research Letters* **49** no. 6, (2022) e2022GL098073.

[68] R. U. Abbasi *et al.*, Telescope Array Collaboration *Journal of Geophysical Research: Atmospheres* **123** no. 13, (2018) 6864–6879.

[69] R. U. Abbasi *et al.*, Telescope Array Collaboration *Geophysical Research Letters* **50** no. 14, (2023) e2023GL102958.

[70] R. Abbasi *PoS* **ICRC2023** (2023) 250.

[71] A. Aab *et al.*, Pierre Auger Collaboration *Earth and Space Science* **7** no. 4, (2020) e2019EA000582.

[72] A. Abdul Halim *et al.*, Pierre Auger Collaboration *PoS* **ICRC2023** (2023) 372.

[73] O. Lux, I. Krisch, O. Reitebuch, D. Huber, D. Wernham, T. Parinello, A. Abdul Halim, *et al.*, Pierre Auger Collaboration *Optica* **submitted to** (2023) , arXiv:2310.08616 [astro-ph.IM].